LANGMUIR

pubs.acs.org/Langmuir Article

# On the Stability of Pickering and Classical Nanoemulsions: Theory and Experiments

Boxin Ding,* Seyedeh Hannaneh Ahmadi, Petro Babak, Steven L. Bryant,* and Apostolos Kantzas*

Cite This: *Langmuir* 2023, 39, 6975–6991 Read Online

ACCESS | Metrics & More | Article Recommendations | Supporting Information



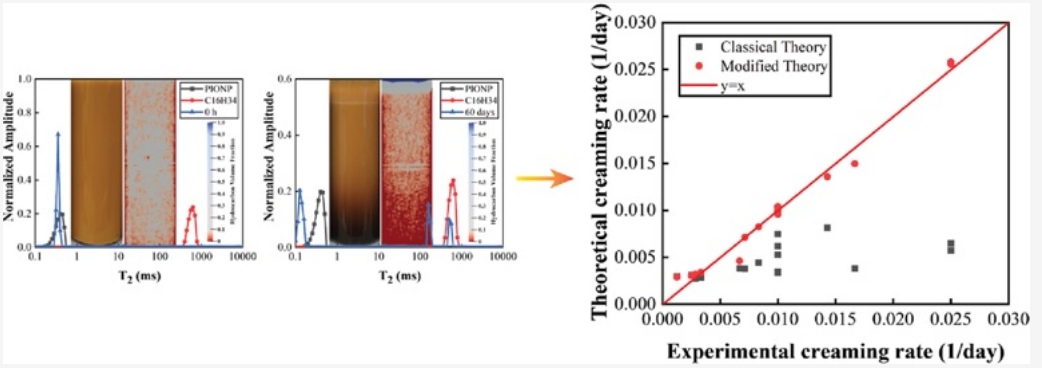


**ABSTRACT:** Emulsification is a crucial technique for mixing immiscible liquids into droplets in various industries, such as food, cosmetics, biomedicine, agrochemistry, and petrochemistry. Quantitative analysis of the stability is pivotal before the utilization of these emulsions. Differences in X-ray attenuation for emulsion components and surface relaxation of the droplets may contribute to X-ray CT imaging and low-field NMR spectroscopy as viable techniques to quantify emulsion stability. In this study, Pickering (stabilized solely by nanoparticles) and Classical (stabilized solely by low molecular weight polymers) nanoemulsions were prepared with a high-energy method. NMR and X-ray CT were employed to constantly monitor the two types of nanoemulsions until phase separation. The creaming rates calculated from NMR match well with the results obtained from X-ray CT. Furthermore, we show that Stokes' law coupled with the classical Lifshitz−Slyozov−Wagner theory underestimates the creaming rate of the nanoemulsions compared to the experimental results from NMR and X-ray CT imaging. A new theory is proposed by fully incorporating the effects of Pickering nanoparticles, hydrocarbon types, volume fraction, size distribution, and flocculation on the droplet coarsening. The theoretical results agree well with the experimentally measured creaming rates. It reveals that the attachment of nanoparticles onto a droplet surface decreases the mass transfer for hydrocarbon molecules to move from the bulk aqueous phase into other droplets, thus slowing the Ostwald ripening. Therefore, Pickering nanoemulsions show a better stability behavior compared to Classical nanoemulsions. The impacts of hydrocarbon and emulsification energy on the stability of nanoemulsions are reported. These findings demonstrate that the stability of the nanoemulsions can be manipulated and optimized for a specific application, setting the stage for subsequent investigations of these nanodroplets.

## INTRODUCTION

There has been considerable interest within the food, biomedical, environmental, petrochemical, and other industries in using emulsions to encapsulate, protect, and deliver nanomaterials and lipophilic components.[1−7] Emulsions generally consist of a dispersion of droplets distributed within the other immiscible liquid medium. Emulsification is usually caused by the reduction of the Gibbs free energy between the two fluids. In terms of the equation of Gibbs free energy, $\Delta G = \Delta A\gamma - T\Delta S$, the reduction usually incorporates the addition of emulsifiers to reduce interfacial tension ($\gamma$) and inputting external energy to compensate for the increases in the interfacial area ($\Delta A$) and the very small entropy of the colloidal dispersion ($T\Delta S$).[8] The emulsions with droplet size on the nanometric scale are referred to as the nanoemulsions[9] and microemulsions.[10] Thermodynamic microemulsions are usually generated with $\Delta G \leq 0$ when $\gamma$ is extremely low, while nanoemulsions are only kinetically stable with $\Delta G > 0$. In some specific applications, it is desirable to utilize nanoemulsions as they offer several potential advantages over macroemulsions and microemulsions. First, the nanoscale droplet size causes the Brownian motion strong enough to prevent flocculation,

Received: January 13, 2023
Revised: April 7, 2023
Published: April 21, 2023

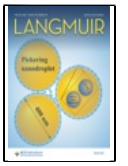




https://doi.org/10.1021/acs.langmuir.3c00133
*Langmuir* 2023, 39, 6975−6991

coalescence, and gravitational separation (i.e., creaming or sedimentation).[11] Therefore, they usually exhibit better stability. Second, nanoemulsions are suitable for the efficient delivery of active ingredients (e.g., drugs, nutraceuticals, cosmetics, environmental amendment agents, and chemical additives for improved oil recovery, etc.) due to their very small size associated with a large specific surface area.[12,13] Third, unlike microemulsions, nanoemulsions can be prepared using a decent concentration of emulsifiers.[14] Fourth, combined effects for specific applications may be achieved when attaching nanomaterials to nanodroplets (i.e., Pickering nanoemulsion[15]), such as nanomaterials to catalyze the chemical degradation of contaminants and oil to encourage microbial degradation for environmental remediation.[16] Fifth, Pickering nanoemulsion can be functionalized for some specific applications, such as magnetic nanodroplets for controllable stability[17] and characterization of fractures in tight reservoirs.[18]

In spite of the above-listed advantages, nanoemulsions have only attracted interest in recent years due to the challenges raised in initially creating nanodroplets and the subsequent stabilization of these nanodroplets against break-up, especially the lack of understanding of the instability of nanoemulsions.[19] The mechanisms of nanoemulsion instability generally include gravity separation (i.e., creaming/separation), coalescence, flocculation, and Ostwald ripening.[20−22] There is a large volume of literature reporting the stability of the nanoemulsions while most of them are examined through "vial screening tests" by visually evaluating the performance of emulsion stability in a transparent vial.[23−26] Limited data and quantitative analysis are not readily available for the characterization of nanoemulsion stability due to the lack of effective analytical and experimental methods. In this study, low-field nuclear magnetic resonance (NMR) relaxometry and X-ray computed tomography (CT) imaging were utilized to provide quantitative insights into the instability of nanoemulsions.

NMR experiments employed the Carr−Purcell−Meiboom−Gill (CPMG) pulse sequence to measure the transverse relaxation time ($T_2$). Peña and Hirasaki[27] first proposed that the CPMG pulse sequence is suitable for evaluating the stability of emulsions. Subsequently, Jiang et al.[28] and Opedal et al.[29] utilized this theory to investigate the stability of the water-in-oil (W/O) emulsion. This pulse sequence generally involves the application of a 90° pulse followed by a series of 180° pulses separated by an echo time. For the measurements in the nanoemulsion samples, two independent relaxation mechanisms are involved, bulk fluid processes and surface relaxation. For nanoemulsions with a certain volume of sphere oil droplets, both processes act in parallel, and $T_2$ is given by[30]

$$\frac{1}{T_2} = \frac{1}{T_{2\text{bulk}}} + \frac{1}{T_{2\text{surface}}} = \frac{1}{T_{2\text{bulk}}} + K\left(\frac{S}{V}\right) = \frac{1}{T_{2\text{bulk}}} + K\frac{3}{r} \quad (1)$$

where $T_{2\text{bulk}}$ is the relaxation time of bulk fluid, $T_{2\text{surface}}$ is the relaxation time resulting from surface relaxation, $K$ is the strength of surface relaxation, and $r$ is the radius of the sphere droplets. Bulk relaxation is the intrinsic relaxation property of a fluid and is dependent on the physical properties of the fluid, such as viscosity and chemical composition. Surface relaxation occurs at the fluid−solid/fluid interface, i.e., surfaces of the nanoparticle and oil droplets. As nanoemulsion becomes unstable under static conditions, the relaxation time of the same sample changes due to the variation of droplet size and phase distribution.[27] Therefore, the instability of the nanoemulsion can be theoretically interpreted by NMR relaxometry. The principle of X-ray CT is the fact that X-rays lose their energy as they pass through a medium, and this reduction depends on the density of the substance and the path length through that substance. In terms of the density difference between the dispersed and continuous phase, X-ray CT can detect the hydrocarbon distribution within the nanoemulsion spatiotemporally. Compared to other techniques, such as light transmission, evaporation, solvent extraction, or turbidity measurements,[31] the NMR and X-ray CT measurements are simple, fast, nondestructive, suitable for analyzing optically opaque nanoemulsions, and capable of yielding an incredible wealth of information in a particular sample.[32]

In this study, the instability of two types of nanoemulsions, Pickering nanoemulsion and Classical nanoemulsion, was investigated experimentally and theoretically. For the Pickering nanoemulsions, in-house engineered iron oxide nanoparticles were utilized as an emulsifier. In contrast, the polymer with the same concentration as the coating onto the surface of the nanoparticles in Pickering nanoemulsion was applied to stabilize Classical nanoemulsion. A total of 16 Pickering and Classical nanoemulsions were monitored, quantified, and their instability was analyzed through low-field NMR spectroscopy and X-ray CT imaging in parallel. The mechanisms of stability on Pickering and Classical nanoemulsions were discussed theoretically. Impacts of hydrocarbon and emulsification energy on the stability of both Pickering and Classical nanoemulsions were investigated. The instability results obtained from low-field NMR and X-ray CT were compared, identified, and validated with the theoretical modeling results.

## EXPERIMENTS

**Materials.** In this study, the nanoemulsions comprised hydrocarbon, Milli-Q water, and an emulsifier. For Pickering nanoemulsion, the emulsifier is engineered iron oxide nanoparticles (IONPs). The bare IONPs ($Fe_3O_4$, 98+%, 20-30 nm, US Research Nanomaterials, Inc.) were coated with a low molecular weight polymer: poly(4-styrenesulfonic acid-*co*-maleic acid) sodium salt-20 kD (PSS-*co*-MA, 0.94 g/mL, Sigma-Aldrich). The Classical nanoemulsions were stabilized by the same concentration of the PSS-*co*-MA polymer as the coating onto the surface of the IONP. In this way, the solid IONP was the only variable when investigating the stability between the Pickering nanoemulsions and the Classical nanoemulsions. Different hydrocarbons were employed as the dispersed oil phase, including *n*-decane ($C_{10}H_{22}$, Sigma-Aldrich), *n*-dodecane ($C_{12}H_{26}$, Sigma-Aldrich), *n*-hexadecane ($C_{16}H_{34}$, Sigma-Aldrich), and 1-octadecene ($C_{18}H_{36}$, Sigma-Aldrich). Hydrochloric acid (HCl, Sigma-Aldrich) and sodium hydroxide (NaOH, Sigma-Aldrich) were applied to adjust the pH value of the aqueous phase.

**Functionalization of IONP.** The magnetic IONPs were first engineered to improve their dispersity and the emulsifiability of dispersed nano-oil-droplets in the continuous water phase (i.e., oil-in-water (O/W) nanoemulsion). 4 wt % PSS-*co*-MA polymer and 1 wt % IONPs were first added in 500 mL of DI water with the pH value adjusted to 5. Then, the aqueous phase was mixed evenly using a homogenizer (VWR 250, VWR Scientific Inc., USA) at a rotation speed of 10,000 RPM. After no visible PSS-*co*-MA polymer and IONP supernatant on the aqueous phase, the polymeric nanofluids were transferred to a probe sonicator (ultrasonic processor, Q700, Qsonica) for 60 min ultrasonication with a pulse on/off time of 30 s/30 s at 50% amplitude in an iced water bath.

In this way, the PSS-*co*-MA polymer molecules can attach well onto the surface of the IONP so that a polymer coating is caged around the IONP core.[33] However, there are still some non-coated IONPs and/or remaining PSS-co-MA polymers in the bulk fluid. To extract the


https://doi.org/10.1021/acs.langmuir.3c00133
Langmuir 2023, 39, 6975−6991

polymer-coated iron oxide nanoparticles (PIONP), the polymeric nanofluids were first centrifuged for 20 min at 4000 RPM to remove the uncoated IONPs. Then, the supernatant was processed by concentrating and washing[18] with DI water using 100 kD centrifugal filter units (AmiconUltra-12, 100 kDa, MilliporeSigma).

After three times centrifuge, the concentrated PIONPs ranged from 20 to 30 wt % in the nanofluid determined using inductively coupled plasma-mass spectrometry (ICP-MS). The Fe content in the IONP core and S content in the PSS-*co*-MA polymer coating were used to evaluate the mass ratio of the polymer to IONP. Then, the concentration of PIONPs in nanofluid can be determined. In addition, thermogravimetric analysis (TGA) was also used to analyze the decomposition of the concentrated PIONP nanofluid and validate the ICP results. The PIONP utilized for emulsification has a polymer coating to bare IONP ratio of 3.9. The polymer-to-nanoparticle (P/N) ratio can be pivotal in emulsification and is discussed thoroughly in the other paper. In this study, the P/N ratio of 3.9 was controlled via utilizing the same sonication period and centrifuge times.

**Generation and Standard Characterization of the Nanoemulsions.** Nanoemulsions were generated by ultrasonication of hydrocarbon in the aqueous phase, i.e., PIONP nanofluid for Pickering nanoemulsions and polymer solution for Classical nanoemulsions. The corresponding polymer concentration in Classical nanoemulsion can be calculated as

$$c = \frac{a}{a+1} \times 100\% \tag{2}$$

where $a$ is the ratio of polymer coating to bare IONP. Ultrasonication was utilized to generate an appropriate oil−water interface area and significantly reduce the oil droplet size to the nanoscale. The sonicator probe has a tip diameter of 3/4″ (19.1 mm), and its amplitude is 60 microns at setting 100%. At setting 35, 40, 45, and 50, the amplitudes are approximately 21, 24, 27, and 30 microns, respectively. The corresponding energies delivered into 100 mL of nanoemulsion in a 200 mL beaker with a constant emulsification time of 60 min are 36, 40, 43, and 48 kJ, respectively.

Generally, the nanoemulsion samples were prepared in a bulk of 100 mL and then transferred into three VWR 50 mL vials with dimensions of 25 mm in diameter and 108 mm in height as well as two 40 mL and one 20 mL vials. All three samples were in VWR 50 mL vials with screw caps to prevent any loss of the emulsion. One of the 40 mL vials was dedicated to NMR measurements, and the other was dedicated to X-ray CT imaging, conducted in parallel. The 20 mL samples were processed with the standard characterization, including morphology, rheological behavior, $\zeta$-potential, and nanodroplet size distribution. The morphologies of the bare IONP and PIONP were analyzed by transmission electron microscopy (TEM), while the nanostructure of the Pickering nanodroplets was imaged by scanning electron cryomicroscopy (CryoSEM). The size distribution and $\zeta$-potential of the nanodroplets were determined through the dynamic light scattering (DLS) method via a NanoPlus HD Particle Size & Zeta Potential Analyzer. The rheological behavior was assessed through a rheometer (Dynamic Shear Rheometer, SmartPave 92, Anton Paar).

**Nanoemulsion Stability Quantification Tests.** The instability of nanoemulsions was monitored and quantified spatiotemporally through a 64 Slice X-ray CT Scanner. For each test, several standard samples were first scanned, and the resultant CT number (also referred to as the Hounsfield scale[34]) was calibrated by samples with known density values under room temperature, approximately 22 °C. The $x-y$ resolution in the plane is 0.195 × 0.195 mm for these experiments. The slice thickness is 0.625 mm, and therefore, the size of each voxel (3-D pixel) in the images is 0.195 × 0.195 × 0.625 $mm^3$. For each scanning, the tested samples were gently transferred to measurable locations to avoid any re-emulsification.

The NMR measurements were performed in parallel with a low-field Maran Ultra Imaging Spectrometer (Oxford Instruments, Abingdon, UK) operating at a frequency of 2.5 MHz (0.058 T). The CPMG pulse sequence was utilized to determine the relaxation time of the sample at a different aging time. Relaxation distributions of all samples were obtained at a constant echo time (TE) of 0.44 ms, waiting time (TW) of 12,000 ms, 32 trains, and pulse number (NE) of 10,000, which produce a signal-to-noise ratio of at least 70 for Pickering nanoemulsions and 300 for Classical nanoemulsions.

In early times, the X-ray CT imaging and NMR measurements were processed every 12 h for the first 72 h after the emulsification. Subsequently, measurements were taken every 1 day, 3 days, and 5 days in sequence until there was little change in the density profile and NMR relaxation distribution. After this critical period, measurements were taken every 10 days until there were no further changes in the density and $T_2$ distributions.

**Interpretation of X-ray CT Slices and NMR Relaxometry.** Interpretation of the X-ray CT slices was first processed with in-house MATLAB codes to generate VTK files.[35] Subsequently, the obtained VTK files were loaded into ParaView for the reconstruction of the 1D profile, 2D distribution, and 3D images. The resultant CT numbers were first translated to density by using the model generated from the standard samples. Then, the density of nanoemulsions was normalized with dispersed hydrocarbon and continuous aqueous phase (i.e., PIONP nanofluid for Pickering nanoemulsion and polymer solution for Classical nanoemulsion):

$$\xi_n = \frac{\rho_m - \rho_d}{\rho_c - \rho_d} \tag{3}$$

where $\xi_n$ is the normalized density, $\rho_m$ is the calculated density of the mixed phase (i.e., nanoemulsion) from the CT slices, $\rho_d$ is the density of the dispersed phase, and $\rho_c$ is the density of the continuous phase. In terms of mass conservation, we have

$$\rho_m V_m = \rho_c V_c + \rho_d V_d \tag{4}$$

where $V_m$ is the volume of the mixed phase, $V_d$ is the volume of the dispersed phase, and $V_c$ is the volume of the continuous phase. Since the continuous phase is immiscible to the dispersed phase, eq 4 can be re-written as

$$\rho_m = \frac{\rho_c V_c + \rho_d V_d}{V_c + V_d} \tag{5}$$

Substituting eq 5 into eq 3 yields

$$\xi_n = 1 - \frac{V_d}{V_c + V_d} = 1 - \phi_o \tag{6}$$

where $\phi_o$ is the hydrocarbon volume fraction of the nanoemulsion. In terms of eq 6, the normalized density is proportional to the oil volume fraction, and therefore, the X-ray CT results can be interpreted as the spatiotemporal hydrocarbon profile.

For interpretation of the NMR relaxation curves, the amplitude in the $T_2$ relaxation distribution refers to the measurable hydrogen protons in the sample, and it is proportional to the same mass.[30] For the NMR relaxation distribution of pure hydrocarbon, the amplitude index can be expressed as

$$I_h = \frac{AP_h}{\rho_h V_h} \tag{7}$$

where $I$ is the amplitude index, AP is the amplitude of the fluid signal, and $\rho$ and $V$ are the density and volume of the fluid, respectively. The subscript, h, represents hydrocarbon. For NMR relaxation distribution of nanoemulsion, the amplitude caused by the oil creaming and free oil is detectable and can be used for calculation of their volume:

$$V_{eo} = \frac{A_{eo}}{\rho_h I_h} \tag{8}$$

where the subscript, eo, represents the oil creaming and free oil in nanoemulsions.

## THEORETICAL MODEL

Nanoemulsions are thermodynamically unstable, and the instability processes include (1) creaming or sedimentation



https://doi.org/10.1021/acs.langmuir.3c00133
Langmuir 2023, 39, 6975−6991

due to the gravity separation; (2) flocculation caused by van der Waals attraction when there is no sufficient repulsion between the droplets; (3) Ostwald ripening resulting from the difference in solubility between the small and large droplets; and (4) coalescence induced by thinning and disruption of the liquid film between the droplets.

Some of the large droplets grow at the expense of the small droplets through the molecular dissolution of the hydrocarbon in the aqueous phase. This instability process is the so-called Ostwald ripening. The rate of Ostwald ripening, $\omega$, has been derived by Lifshitz, Slezov, and Wagner (also referred to as the LSW theory):[36,37]

$$\omega = \frac{dr^3}{dt} = \frac{8}{9}\frac{S_\infty \sigma v_m D}{\rho_o RT} \tag{9}$$

where $D$ is the diffusion coefficient of the dispersed phase in the continuous phase, $S_\infty$ is the solubility of the hydrocarbon, $\sigma$ is the interfacial tension between the dispersed droplets and continuous medium, $v_m$ is the molar volume of the dispersed phase, $\rho_o$ is the density of the dispersed phase, $R$ is the gas constant, and $T$ is the absolute temperature. Equation 9 describes the Ostwald ripening rate of Classical nanoemulsions. Pickering nanoemulsions distinguish the Classical nanoemulsions from the adsorbed Pickering nanoparticles on the droplet surface. These Pickering nanoparticles act as a barrier to decrease the surface area exposed to the continuous water media; therefore, the mass transfer for hydrocarbon molecules to move from the bulk aqueous media into the droplets is inhibited compared to the Classical nanoemulsions.[38,39] These mechanics can be incorporated into eq 9 by introducing two inhibition coefficients:

$$\omega = \frac{8}{9}\frac{S_\infty}{\theta}\frac{\sigma v_m}{\rho_o RT}\lambda D \tag{10}$$

where $\lambda$ is the average covering coefficient, ranging between 0 and 1. $\theta$ is the solubility inhibition coefficient, which is larger than 1. When more nanoparticles are attached to the droplet surface, the average covering coefficient decreases, and the solubility inhibition coefficient increases; therefore, the rate of Ostwald ripening becomes smaller in Pickering nanoemulsions.

Furthermore, the individual emulsion droplets can also aggregate together by adhering to each other to form a large oil cluster. The flocculation can be explained by the Derjaguin–Landau–Verwey–Overbeek (also referred to as the DLVO theory):[36,40,41]

$$E_t = E_d + E_e = -\frac{rA_H}{12H} + 32\pi r\varepsilon\left(\frac{k_b T}{e}\right)^2\left[\tanh\left(\frac{e\psi_0}{4k_b T}\right)\right]^2 e^{-kH} \tag{11}$$

where $E_t$ is the net potential energy for the interaction between two droplets, $E_d$ is the van der Waals attractive energy, $E_e$ is the repulsive electrostatic energy, $A_H$ is the Hamaker constant for colloidal dispersion, $H$ is the surface-to-surface separation between the droplets, $\varepsilon$ is the permittivity of the aqueous phase, $\psi_0$ is the surface potential (often substituted by the zeta potential $\xi$) and $k$ is the inverse Debye length (or the reciprocal of the double layer thickness), $k_b$ is Boltzmann's constant, and $T$ is the temperature. The DLVO theory proposes that an energy barrier resulting from the repulsive force prevents two droplets from approaching one another and adhering together. But, if the droplets collide with sufficient energy to overcome this energy barrier, the attractive force will pull them into contact where they adhere strongly and irreversibly together to form the flocculation.

Once the droplets are contacted through flocculation or creaming, several oil droplets can combine into a large oil ganglion by coalescence, in which the water films between the droplets are ruptured. The coalescence rate follows a first-order kinetics:[42,43]

$$n = \left(\frac{n_0}{Ct}\right)(1 - e^{-Ct}) \tag{12}$$

where $n$ is the droplet number after coalescence, $n_0$ is the number of droplets immediately after emulsification, $t$ is the aging time, and $C$ is the coalescence rate.

Generally, the individual nanodroplets first undergo flocculation or/and Ostwald ripening, and the resultant micro-scale droplets have their Stokes motion exceeding the Brownian diffusion, resulting in creaming.[42] For very dilute emulsions (volume fraction $\phi < 0.01$), the rate of creaming follows Stokes' law:[42]

$$v_o = \frac{2r^2\Delta\rho g}{9\mu_w} \tag{13}$$

where $\mu_w$ is the viscosity of the continuous water media, $r$ is the droplet radius, $\Delta\rho$ is the density difference between the dispersed droplets and the continuous phase, and $g$ is the gravity acceleration.

For a more concentrated emulsion system ($0.1 \le \phi \le 0.2$), the creaming rate is reduced below the Stokes' rate:[42]

$$v_e = v_o(1 - 6.55\phi) \tag{14}$$

where $\phi$ is the volume fraction of the dispersed phase.

Furthermore, the flocculation and Ostwald ripening accelerate the creaming rate by increasing the droplet size in a whole emulsion system. It is known that the Ostwald ripening is the dominant mechanism of instability for the nanoemulsions.[11,19,20] In terms of the Ostwald ripening, there exists a critical droplet size, $r_c$, where the droplets neither grow nor decrease in size. On the basis of the LSW theory,[36,37] the critical droplet size within a certain nanoemulsion can be written as

$$r_c^3 = r_0^3 + \frac{8}{9}\frac{S_\infty}{\theta}\frac{\sigma v_m}{\rho_o RT}\lambda D t_c \tag{15}$$

where $t_c$ is the time when the droplet size reaches the critical size from the original size, $r_0$. However, the classical LSW theory is known to underestimate the coarsening rates of the whole emulsion system.[19,39,44] Weiss et al.[39] attributed the faster-coarsening rates to the enhanced transport of the hydrocarbon via micellar dissolution. Furthermore, the volume fraction and initial size distribution of the emulsion are not considered in the LSW theory, which has been found to play a significant role in the coarsening rates.[45]

In addition, several droplets adhere together to form flocs, thus increasing the critical droplet size. This results in a faster creaming rate. Therefore, eq 15 can be modified by introducing a distribution coefficient:

$$r_c = a\left(r_0^3 + \frac{8}{9}\frac{S_\infty}{\theta}\frac{\sigma v_m}{\rho_o RT}\lambda D t_c\right)^{1/3} \tag{16}$$



https://doi.org/10.1021/acs.langmuir.3c00133
Langmuir 2023, 39, 6975−6991

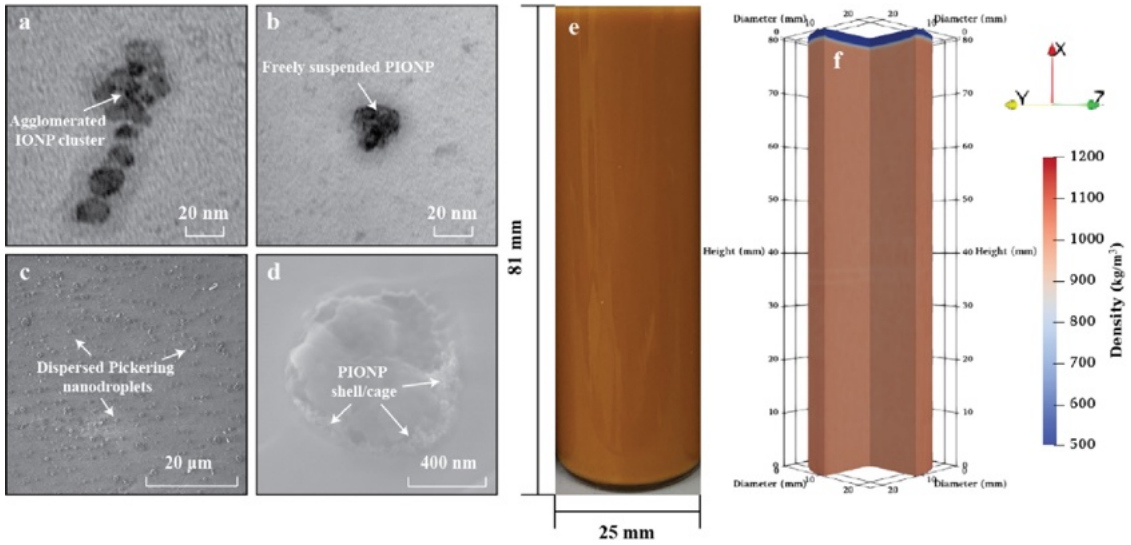


**Figure 1.** Morphology of the nanoparticles and nanodroplets: (a) TEM image of bare/non-coated IONPs; (b) TEM image of a PIONP; (c) CryoSEM image of Pickering nanoemulsion; (d) CryoSEM image of an individual Pickering nanodroplet; (e) screening photo of bulk Pickering nanoemulsion; and (f) 3D reconstructed CT image of bulk Pickering nanoemulsion.

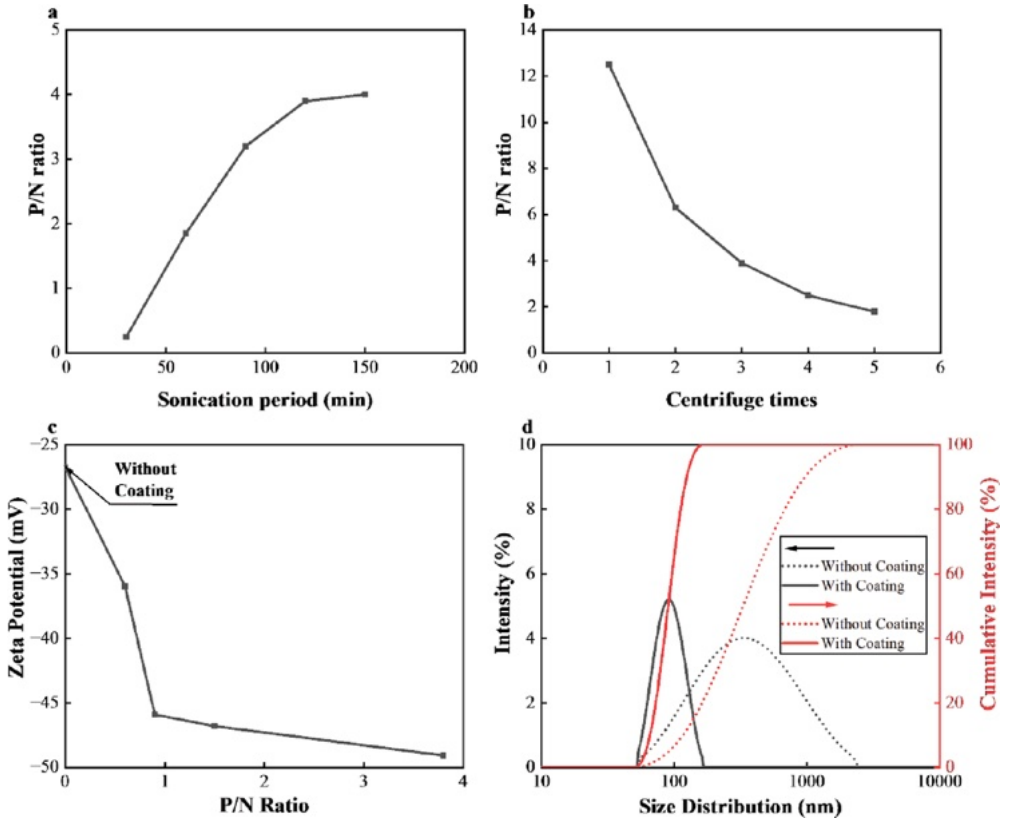


**Figure 2.** Characterization of iron oxide nanoparticles: (a) Polymer-to-nanoparticle (P/N) ratio as a function of sonication period; (b) P/N ratio as a function of centrifuge times; (c) zeta potential as a function of P/N; and (d) size distribution.

The distribution coefficient, *a*, should be larger than 1. When the flocculation is more significant, *a* becomes larger and vice versa.

Substituting eqs 16 and 13 into eq 14, the average creaming rate for a whole emulsion system can be described as

$$v_e = \frac{2\Delta\rho g(1 - 6.55\phi)}{9\mu_w}\left[r_0^3 + \frac{8}{9}\frac{S_\infty}{\theta}\frac{\sigma v_m}{\rho_o RT}\lambda D t_c\right]^{2/3} \quad (17)$$

Equation 17 describes an average creaming rate for a specific nanoemulsion stabilized by either Pickering particles or Classical emulsifiers (i.e., surfactants, alkalis, and polymers.). The viscosity, density, solubility, and interfacial tension (IFT) of hydrocarbon refer to the PubChem and data sheet from the suppliers. The diffusion coefficient of the hydrocarbon is calculated based on the Stokes−Einstein equation.[46] All the



https://doi.org/10.1021/acs.langmuir.3c00133
Langmuir 2023, 39, 6975−6991

experimental data and numerical coefficients for theoretical modeling are listed in Table S1 in the Supporting Information.

## RESULTS AND DISCUSSIONS

**Characterization of Nanoemulsion.** Having generated Pickering and Classical nanoemulsions with different hydrocarbons and emulsification energies, each of the 16 nanoemulsions was characterized through their morphology, droplet size distributions, rheological behavior, and ζ-potential in parallel with the stability experiments by X-ray CT imaging and NMR relaxometry.

The structural characterization of the nanoparticle, nanodroplets, and bulk of Pickering nanoemulsion is depicted in Figure 1. As shown in Figure 1a, the bare IONPs are easily aggregated to form a large agglomeration. After the synthesis of IONPs with polymer coating, the PIONPs can suspend well in the water without any agglomeration, as shown in Figure 1b. This is because the polymer coating enhances the electrostatic repulsion of the nanoparticles, and therefore, the PIONPs rebound when the interparticle gets close and remains dispersed within the aqueous medium. Figure 1c shows two dispersed Pickering nanodroplets where their surface is adherent with the PIONPs. These adherent PIONPs form a cage structure around the nanodroplets and protect them from flocculation and coalescence, as shown in Figure 1d. Figure 1e shows the visual observation of the bulk Pickering nanoemulsion. The 40 mL of nanoemulsions has a height of 81 mm in the vial with a diameter of 25 mm. Figure 1f shows the reconstructed 3D CT image with the same dimension as the physical model.

Figure 2a,b shows the polymer-to-nanoparticle (P/N) ratio as the synthesis process changes. For different sonication periods, the centrifuge was conducted 4 times consistently, while a sonication period of 120 min was applied for the investigation of different centrifuge times. In Figure 2a,b, the P/N ratio increases as the sonication period increases, while it decreases with decreasing centrifuge times. This shows that the long sonication period is helpful for the polymer molecules to attach onto the surface of the nanoparticle. In contrast, the attached polymer molecules can be removed from the nanoparticle surface by increasing the centrifuge times. Figure 2c,d shows the characterization of iron oxide nanoparticles before and after coating with polymer molecules. The ζ-potentials decrease from −27 to −49 mV, showing that the polymer-coated iron oxide nanoparticle (PIONP) exhibits greater stability compared to the iron oxide nanoparticle (IONP) without the coatings, as shown in Figure 2c. Figure 2d shows that the PIONP has a size ranging between 60 and 120 nm with a median size approximately 97 nm while the IONP has a wider and larger size ranging between 60 and 4500 nm with a median size of around 820 nm. This is because the bare IONPs are easily aggregated to form a large agglomeration while the PIONPs can suspend well in the water without any agglomerations.

Figure 3 shows the droplet size distribution of different nanoemulsions. As shown in Figure 3a,b, the nanoemulsions with different hydrocarbons exhibit the same distribution. This is achieved by applying longer emulsification periods for hydrocarbons with greater viscosity.[47] For the nanoemulsions with the same hydrocarbon but different emulsification energy, there exists an optimal emulsification energy for the generation of small droplet size with narrow distribution, as shown in Figure 3c,d. For example, the optimum emulsification energy

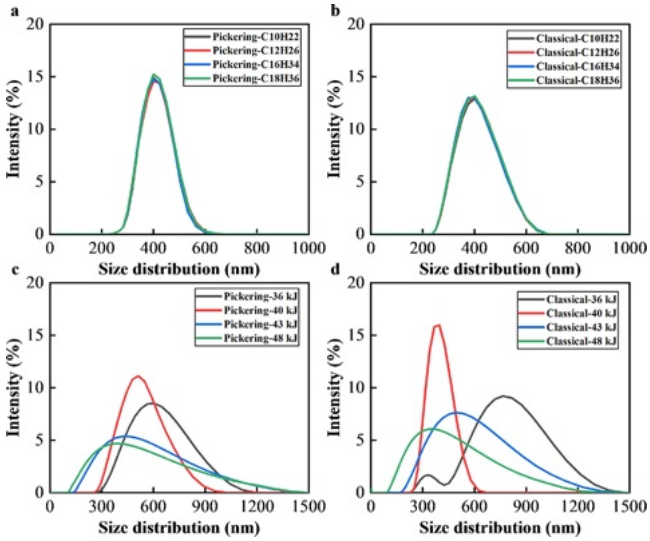


**Figure 3.** Droplet size distribution of different nanoemulsions: (a) Pickering nanoemulsions synthesized with different hydrocarbons; (b) Classical nanoemulsions synthesized with different hydrocarbons; (c) Pickering nanoemulsions synthesized with different emulsification energies; and (d) Classical nanoemulsions synthesized with different emulsification energies.

of 40 kJ produces Pickering nanoemulsion with a narrow size range between 300 and 950 nm and a small median size of 400 nm. However, the emulsification energy smaller than the optimum value contributes a wider size ranging between 300 and 1200 nm with a greater median droplet size of 600 nm. Although the emulsification energy higher than the optimum value can contribute to a small median droplet size of 300 nm, the size distribution becomes wider from 150 to 1500 nm. This results from the fact that the small droplet generates a greater surface-to-volume ratio than the large droplet. The enormous surface area onto the small nanodroplets carries most of the nanoparticles in the system, and thereby, the remaining portion of the nanoparticles can only stabilize the large droplet.

Figure 4 shows the rheology of different nanoemulsions. Within the range of shear rates between 40 and 160 $s^{-1}$, all nanoemulsions, including Pickering nanoemulsions and Classical nanoemulsions, behave as Newtonian fluids in which the viscosity does not change as a function of shear rate. Their bulk viscosities are slightly larger than the viscosities of the continuous aqueous media. Regardless of different hydrocarbons and emulsification energies, Pickering nanoemulsions have a greater viscosity than Classical nanoemulsions. This results from the fact that the coherent nanoparticle shell onto the nanodroplet surface restricts the motion of the Pickering nanoemulsions by exhibiting an increasing bulk viscosity. Figure 4a shows that the hydrocarbons have very limited impacts on the bulk viscosity of the nanoemulsions while small and narrow size distribution contributes to a slightly greater bulk viscosity, as shown in Figure 4b.

Figure 5 shows that the ζ-potentials of all nanoemulsions are negative. The negative values of the hydrocarbon droplet are caused by the emulsifiers onto the droplet surface, i.e., the adherent nanoparticle shell and polymer molecules. Figure 5a shows that the ζ-potential of the nanoemulsion decreases as the carbon chain of the alkane becomes longer while slightly bouncing back with the long carbon chain of octadecene.


https://doi.org/10.1021/acs.langmuir.3c00133
Langmuir 2023, 39, 6975−6991

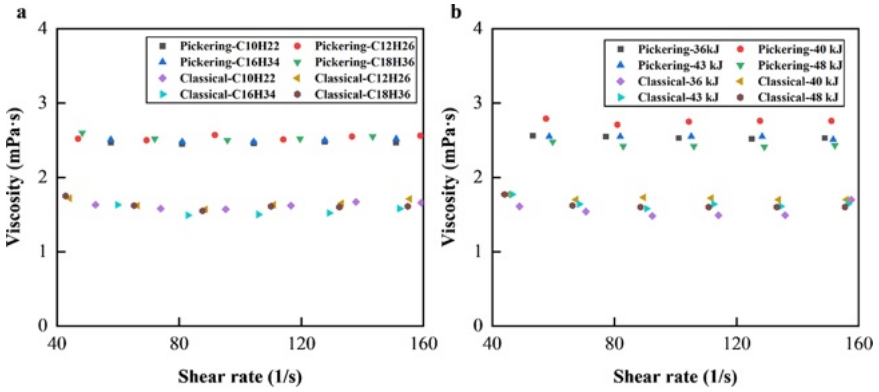


**Figure 4.** Rheology of different nanoemulsions: (a) nanoemulsions synthesized with different hydrocarbons and (b) nanoemulsions synthesized with different emulsification energies.

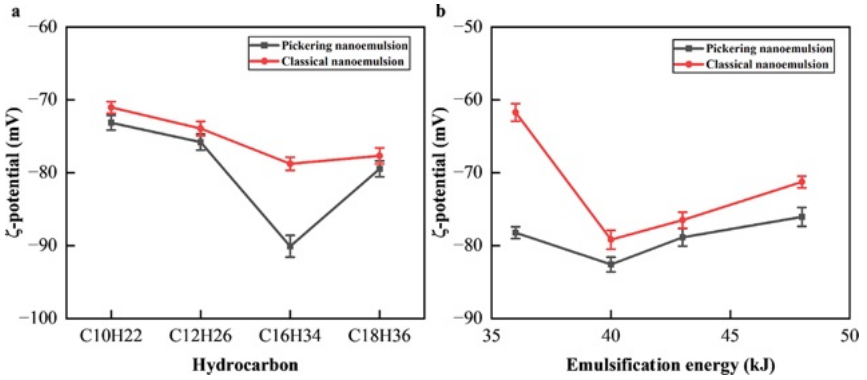


**Figure 5.** ζ-potential of different nanoemulsions: (a) nanoemulsions synthesized with different hydrocarbons and (b) nanoemulsions synthesized with different emulsification energies.

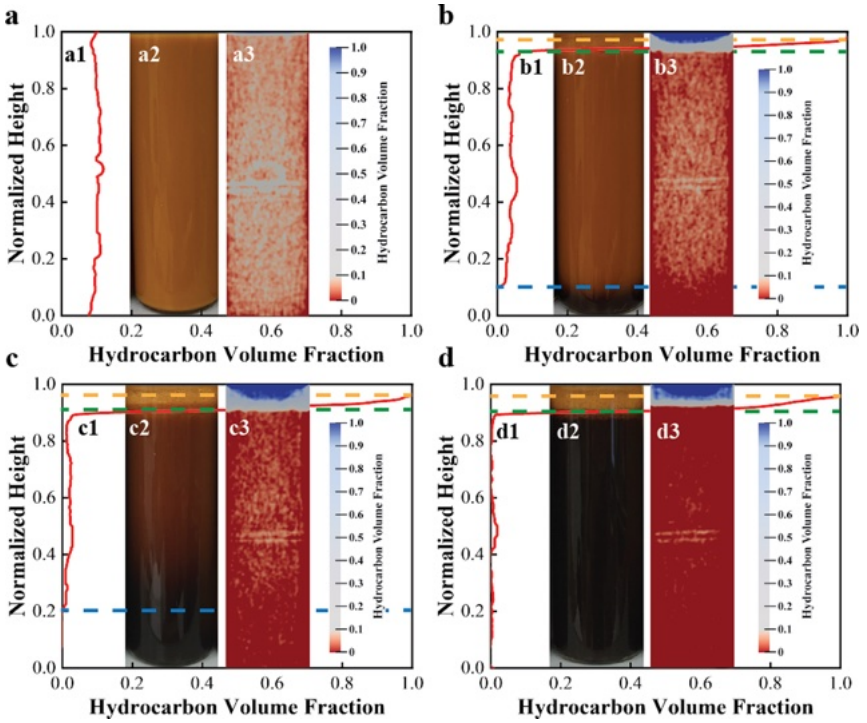


**Figure 6.** Instability of Pickering nanoemulsion synthesized with dodecane at different aging times: (a) 0 h.; (b) 4 days; (c) 15 days; and (d) 60 days. (1)−(3) are the 1D hydrocarbon profile, screening photo, and 2D hydrocarbon distribution, respectively. The orange dashed line shows the boundary between pure hydrocarbon and creaming. The green dashed line represents the boundary between creaming and nanoemulsion, while the blue dashed line describes the boundary between nanoemulsion and nanofluid.



https://doi.org/10.1021/acs.langmuir.3c00133
Langmuir 2023, 39, 6975−6991

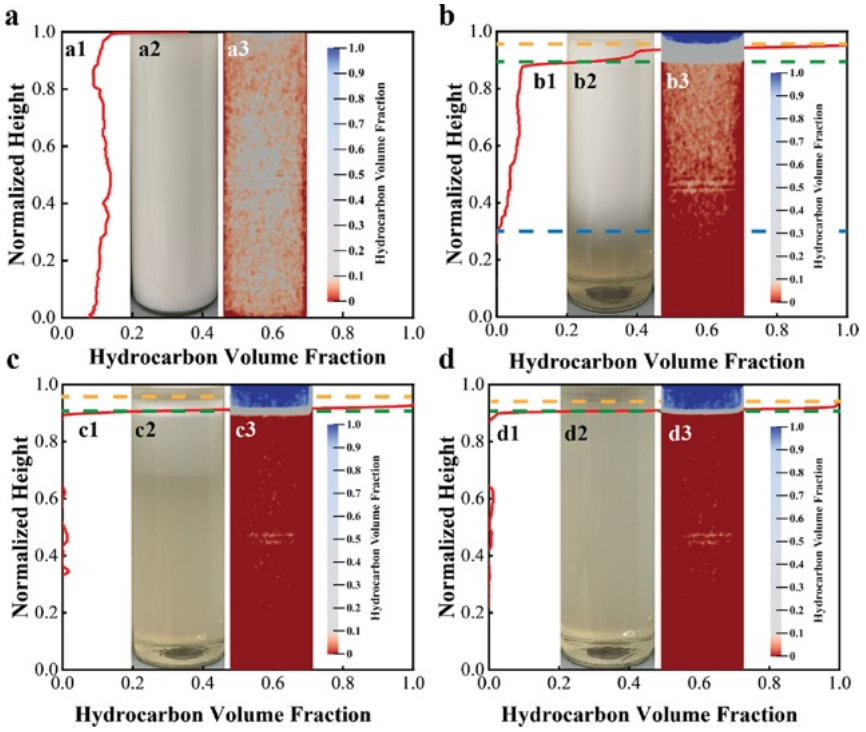


**Figure 7.** Instability of Classical nanoemulsion synthesized with dodecane at different aging times: (a) 0 h; (b) 4 days; (c) 15 days; and (d) 60 days. (1)−(3) are the 1D hydrocarbon profile, screening photo, and 2D hydrocarbon distribution, respectively. The orange dashed line shows the boundary between pure hydrocarbon and creaming. The green dashed line represents the boundary between creaming and nanoemulsion, while the blue dashed line describes the boundary between nanoemulsion and nanofluid.

Figure 5b shows that the optimum emulsification energy for the generation of small size with narrow distribution contributes the smallest $\zeta$-potential. The absolute value of $\zeta$-potential is a crucial factor that describes the electrostatic forces between the nanodroplets, thus further controlling the interactions between nanodroplets. The greater the absolute value, the more nanodroplets tend to repel each other. The stability of these nanoemulsions is analyzed in the next sections.

**Quantification of Nanoemulsion Stability through X-ray CT Imaging.** In this study, we utilized low-field NMR relaxometry and X-ray CT imaging to analyze the instability of the nanoemulsions quantitatively and mechanistically. The advanced characterization of nanoemulsion stability through X-ray CT imaging is first introduced and discussed. Visual observation, 1D hydrocarbon profile, and 2D hydrocarbon distribution are compared, identified, and discussed.

An example of Pickering nanoemulsion synthesized with dodecane is shown in Figure 6. The results for other samples with all aging days are shown in Figures S1−S4 in the Supporting Information. Figure 6a−d presents the nanoemulsion aging for 0 h (i.e., immediately after the emulsification), 4 days, 15 days, and 60 days, respectively. The visual observation can only detect the gravity separation of the nanoemulsions, as shown in Figure 6a2−d2, while the spatiotemporal hydrocarbon profile can be accurately distinguished by X-ray CT imaging in Figure 6a1−d1,a3−d3. Immediately after the emulsification, the hydrocarbon exhibits a homogeneous profile with a volume fraction of 0.1 along the height. After the nanoemulsion ages for 4 days, four sections are separated by three boundaries, including nanofluid, nanoemulsion, creaming, and pure hydrocarbon from the bottom to the top. The boundary between pure hydrocarbon and creaming and the boundary between nanoemulsion and nanofluid are convex to the bottom, while the boundary between creaming and nanoemulsion shows a sinuous instability behavior. When the aging time is extended to 15 days, more droplets move from the nanoemulsion section to the creaming section. The Ostwald ripening leads to the large droplets growing at the expense of the small droplets. This results in the nanoparticles being released from the consumed small droplets' surface and subsequently suspended in the continuous water media. Since these nanoparticles are functionalized with polymer coating, the electrostatic repulsion is sufficiently high to prevent them from agglomerating and accumulating at the bottom. Conversely, the growing droplets with a larger diameter and greater density difference between the dispersed phase and continuous phase make them more easily creaming in terms of eq 17. At the end of the test, only a few droplets were residual in the aqueous phase characterized from the X-ray CT while this cannot be visually observed by the "bottle screening test". Since these residual droplets are well protected by the nanoparticles, they have very limited density differences with the continuous medium to avoid gravity separation, and the adherent particle layer also overcomes the flocculation and Ostwald ripening. As the Pickering nanoemulsion becomes unstable, the top pure hydrocarbon section becomes larger due to the coalescence of the creaming. However, this process is far slower than the Classical nanoemulsions.

Take Classical nanoemulsion synthesized with dodecane as an example, as shown in Figure 7. Similar to the fresh Pickering nanoemulsion, the nanodroplets of the Classical nanoemulsions distribute homogeneously within the system, as shown in Figure 7a1,a3. Visual observation shows that the Classical nanoemulsion exhibits a milky color in Figure 7a2.


https://doi.org/10.1021/acs.langmuir.3c00133
Langmuir 2023, 39, 6975−6991

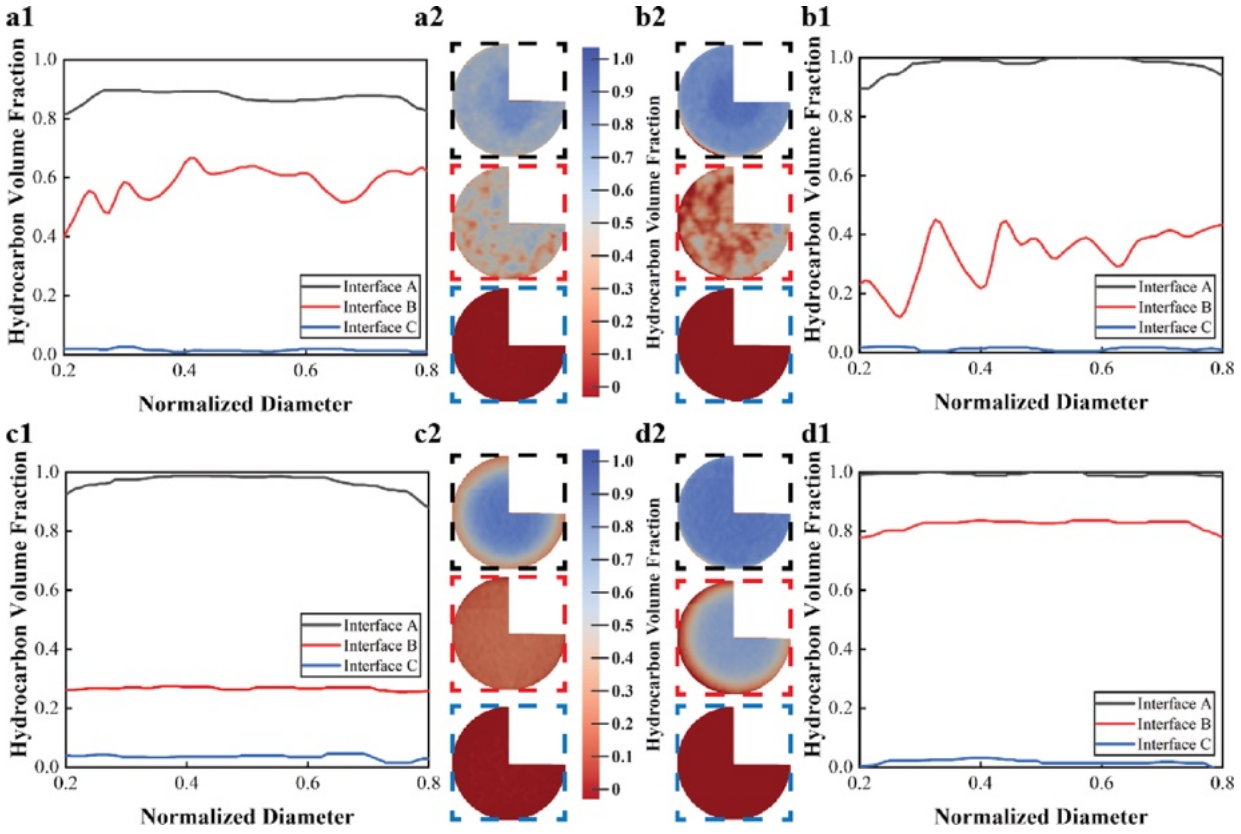


**Figure 8.** Cross section of the boundaries at different aging times: (a) Pickering nanoemulsion at 4 days; (b) Pickering nanoemulsion at 60 days; (c) Classical nanoemulsion at 4 days; and (d) Classical nanoemulsion at 60 days. Boundary A describes the boundary between pure hydrocarbon and creaming. Boundary B represents the boundary between creaming and nanoemulsion, while boundary C shows the boundary between nanoemulsion and nanofluid.

However, Classical nanoemulsion exhibits a less stable behavior, relative to the Pickering nanoemulsions. As the Classical nanoemulsion ages for 4 days, the milky section floats upward in the middle section, leaving the polymer solution at the bottom and the oil-rich section at the top, as shown in Figure 7b2. It is clearly shown in Figure 7b1,b3 that the instability of the Classical nanoemulsion can be divided into four sections, including polymer solution, Classical nanoemulsion, creaming, and pure hydrocarbon from the bottom to the top. When the aging time is extended to 15 days, the nanoemulsion section vanishes with only a few residual nanodroplets distributed near the boundary between creaming and polymer solution, as shown in Figure 7c. In Figure 7c1,c3, the creaming section becomes thinner, with the corresponding section of pure hydrocarbon growing significantly. After the Classical nanoemulsion ages for 60 days, the phase separation is nearly achieved with only a thinner layer of creaming between the pure hydrocarbon and polymer solution.

Comparing the 2D CT images in Figure 6b3−d3 and Figure 7b3−d3, a boundary instability is observed in the Pickering nanoemulsion. We capture the cross sections for the three boundaries and delineate the hydrocarbon distribution among the three boundaries, as shown in Figure 8. To avoid the beam hardening effect[48] when an X-ray beam travels through the vial with a greater density, we only choose the effective profile with the range of normalized diameters between 0.2 and 0.8. In Figure 8a,b, the Pickering nanoemulsion shows a strong instability at boundary B while exhibiting a very smooth curvature at boundaries A and C. However, this instability phenomenon is not captured in the Classical nanoemulsion, where the hydrocarbon profile is homogeneous across the diameter, as shown in Figure 7c,d. This instability at boundary B is caused by the density difference between the nanoparticle (∼5.0 g/cm$^3$) and hydrocarbon (∼0.75 g/cm$^3$) in the Pickering nanoemulsion. Such a huge density difference causes convective mixing and results in the Rayleigh−Taylor instability[49,50] at the boundary of oil creaming and nanoemulsion.

Based on the partitioning delineated in Figures 6 and 7, the spatiotemporal hydrocarbon distribution within the nanoemulsions is determined by sectioning the emulsions. The detailed procedure for determination of the boundary between different sections is provided in the Supporting Information. The evolutional section heights for Pickering and Classical nanoemulsions with different hydrocarbons and emulsification energies are depicted in Figure 9. In Figure 9, all nanoemulsions show an increasing height of the nanofluid section (Figure 9a1−d1), a decreasing height of the nanoemulsion section (Figure 9a2−d2), and an increasing height of the free oil section (Figure 9a4−d4). For the creaming section, we observe an increasing trend with a maximum limit in Pickering nanoemulsions while a parabolic trend in Classical nanoemulsions. In comparison with the Classical nanoemulsions, gravity separation (nanoparticle and oil) and coalescence are relatively slower in Pickering nanoemulsions. This is caused by the significantly strong energy required to remove the particle than to remove the adsorbed polymer molecules from the interface.[51,52] Such energy considerations ensure the stability


https://doi.org/10.1021/acs.langmuir.3c00133
Langmuir 2023, 39, 6975−6991

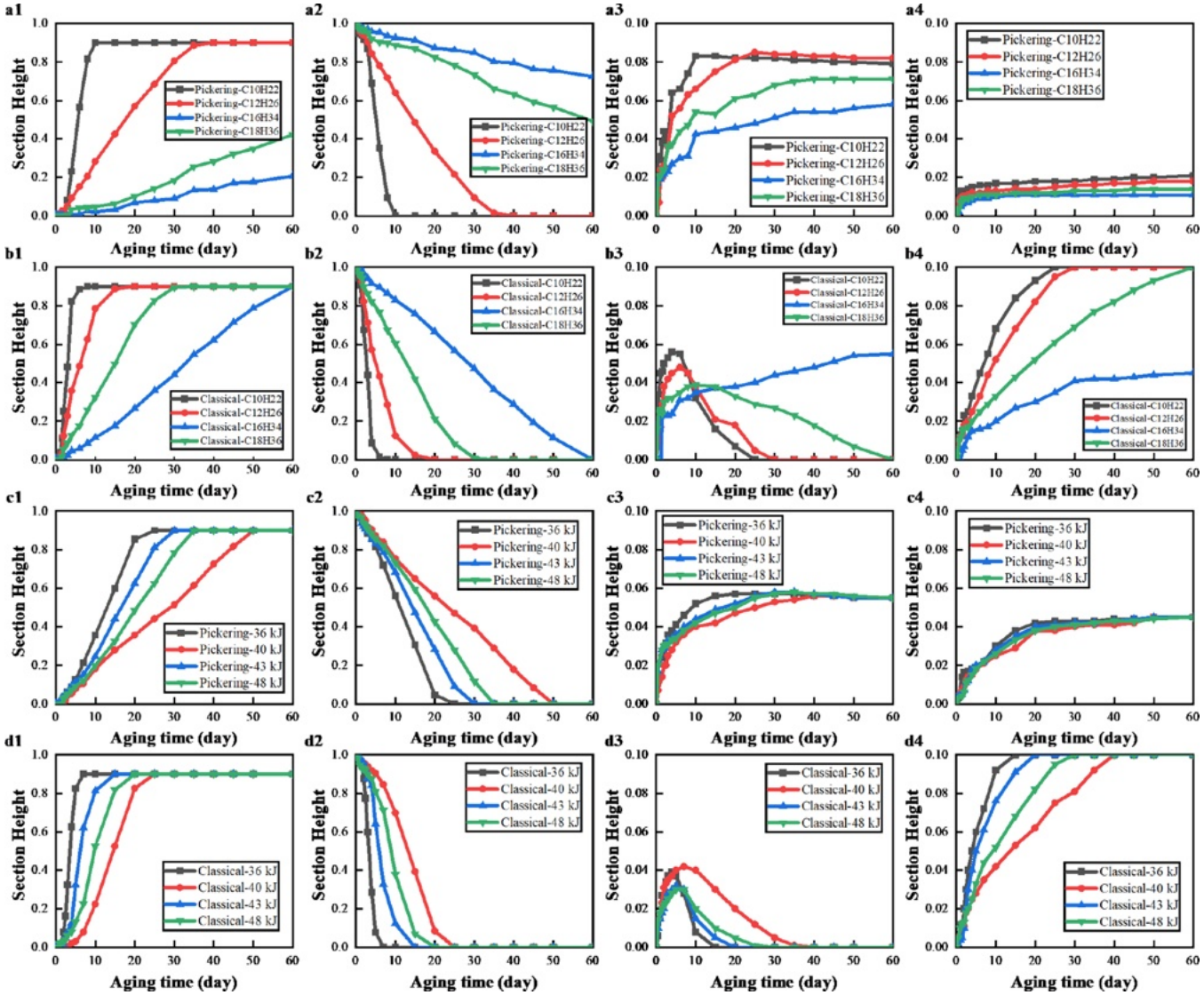


**Figure 9.** Spatiotemporal section heights for different nanoemulsions: (a) Pickering nanoemulsions with different hydrocarbons; (b) Classical nanoemulsions with different hydrocarbons; (c) Pickering nanoemulsions with different emulsification energies; and (d) Classical nanoemulsions with different emulsification energies. (1)−(4) represent the sections of nanofluids/polymer solution, nanoemulsion, oil creaming, and free oil, respectively.

of the Pickering nanodroplets.[53] The polymer coatings of the PIONPs crosslink through side branches or bind to other polymer chains through the electrostatic interactions involving their carboxylate groups ($RCOO^-$). These crosslinked PIONPs are adherent around the nanodroplets, introducing a cage structure that acts as an electrosteric barrier against creaming and coalescence of the armored nanodroplets. More importantly, the nanoparticles attached to the droplet surface can inhibit the transport of the hydrocarbon through molecular diffusion from the bulk aqueous media to other large droplets, i.e., the Ostwald ripening is inhibited with the existence of the nanoparticles. For the Classical nanoemulsions, the presence of excess polymer molecules in the continuous phase can result in a small enhancement (2−3 times) in the rate of Ostwald ripening, presumably by micellar dissolution and transport of the hydrocarbon.[39,54] With the adherent PIONP layer on the nanodroplets, the greater $\xi$-potential (as shown in Figure 5) than that of Classical nanoemulsion contributes a greater repulsive electrostatic energy that prevents the Pickering nanodroplets from flocculation. The abovementioned rigid film generated by the Pickering nanoparticles is also beneficial to slow the coalescence rate compared to Classical nanoemulsions, and thereby the volume of free hydrocarbon at the top of the Pickering nanoemulsion is far less than that of the Classical nanoemulsions.

Due to the very small droplet size associated with a high surface-to-volume ratio, Ostwald ripening is the dominant instability mechanism for the nanoemulsions.[55] Therefore, the Pickering and Classical nanoemulsions synthesized with hydrocarbons with low solubility exhibit better stability compared to those emulsified hydrocarbons with high solubility, as shown in Figure 9a,b. The solubility of the oil in the continuous phase has a major impact on physical stability, with Ostwald ripening rates being directly proportional to oil molar volume in terms of eq 16. The insolubility of hexadecane and octadecene in water acts as a kinetic barrier to Ostwald ripening, making those two nanoemulsions, both the Pickering and Classical ones, inherently stable against Ostwald


https://doi.org/10.1021/acs.langmuir.3c00133
Langmuir 2023, 39, 6975−6991

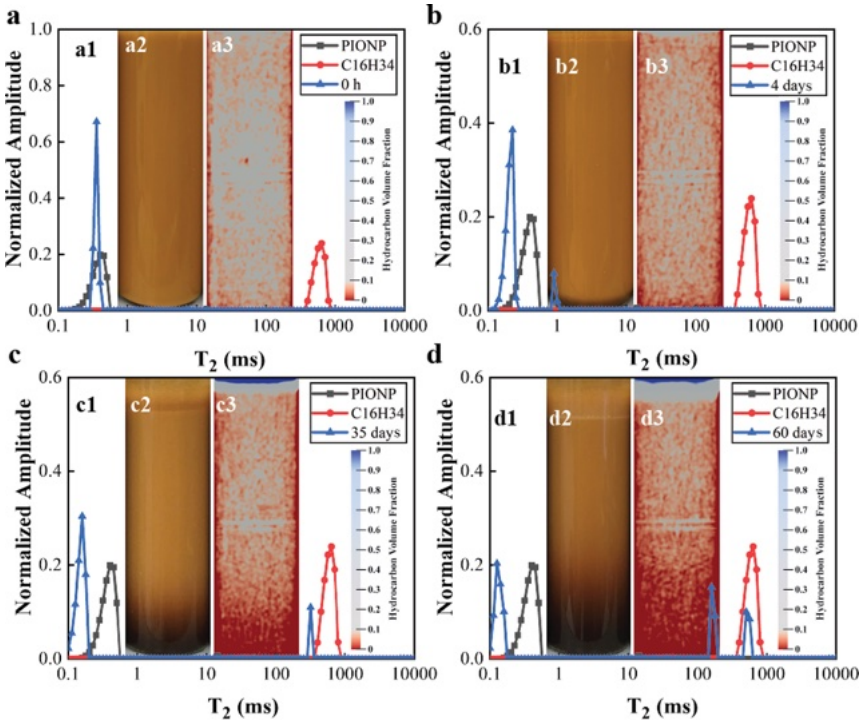


**Figure 10.** Instability of Pickering nanoemulsion synthesized with hexadecane at different aging times: (a) 0 h; (b) 4 days; (c) 35 days; and (d) 60 days. (1)−(3) are the 1D hydrocarbon profile, screening photo, and 2D hydrocarbon distribution. The orange dashed line shows the boundary between pure hydrocarbon and creaming. The green dashed line represents the boundary between creaming and nanoemulsion, while the blue dashed line describes the boundary between nanoemulsion and nanofluid.

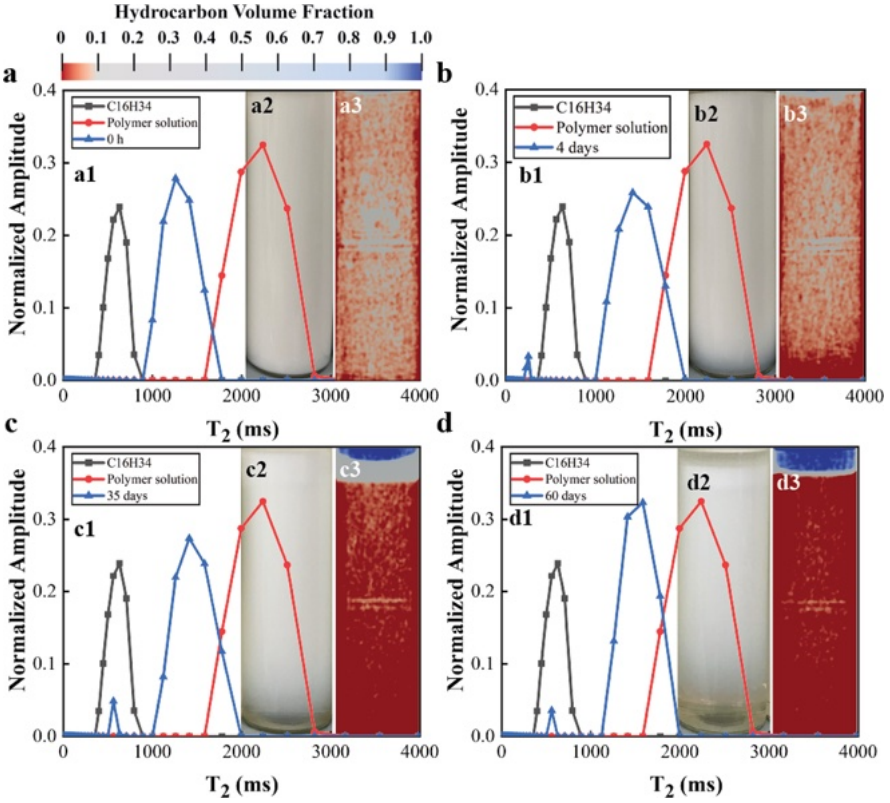


**Figure 11.** Instability of Classical nanoemulsion synthesized with hexadecane at different aging times: (a) 0 h; (b) 4 days; (c) 35 days; and (d) 60 days. (1)−(3) are the 1D hydrocarbon profile, screening photo, and 2D hydrocarbon distribution. The orange dashed line simulates the boundary between pure hydrocarbon and creaming. The green dashed line represents the boundary between creaming and nanoemulsion, while the blue dashed line describes the boundary between nanoemulsion and nanofluid.



https://doi.org/10.1021/acs.langmuir.3c00133
Langmuir 2023, 39, 6975−6991

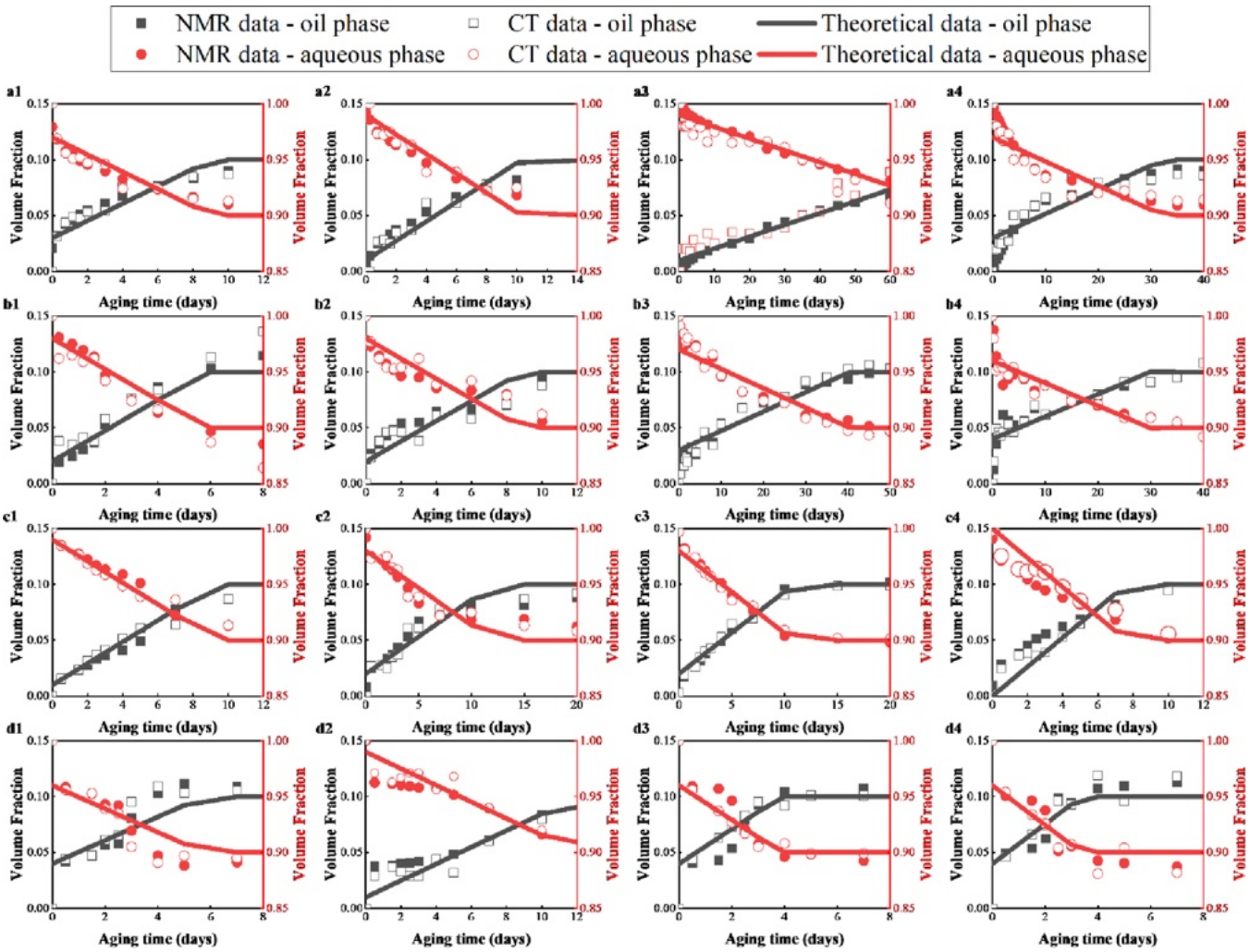


**Figure 12.** Evolutional section heights for different nanoemulsions: (a) Pickering nanoemulsions with different hydrocarbons; (b) Classical nanoemulsions with different hydrocarbons; (c) Pickering nanoemulsions with different emulsification energies; (d) Classical nanoemulsions with different emulsification energies. (1)−(4) represent the different hydrocarbons and emulsification energies: (1) $C_{10}H_{22}$ or 36 kJ; (2) $C_{12}H_{26}$ or 40 kJ; (3) $C_{16}H_{34}$ or 43 kJ; and (4) $C_{18}H_{36}$ or 48 kJ.

ripening. Different hydrocarbons also contribute to different density differences and viscosities. Figure 9c,d shows that there exists optimum emulsification energy, making the nanoemulsions more stable than those below and above this energy. Since the Ostwald ripening arises from emulsion polydispersity and the difference in solubility between small and large droplets, the optimal emulsification energy to generate small droplet size with narrow distribution contributes to the best stability behavior.

**Quantification of Nanoemulsion Stability through Low-Field NMR Relaxometry.** The NMR relaxation distributions for instability of Pickering nanoemulsion synthesized with dodecane are reported, as shown in Figure 10. The results for the remaining samples with all aging days are included in Figures S5−S8 in the Supporting Information. The relaxation distribution of the Pickering nanoemulsions is compared with the PIONP nanofluid (continuous media) and the hydrocarbon (dispersed phase). Figure 10a−d shows the Pickering nanoemulsion aging for 0 h (i.e., immediately after the emulsification), 4 days, 35 days, and 60 days, respectively. The NMR relaxation distributions of the Pickering nanoemulsion are complementary to the visual photo and 2D CT image for the analysis. It is reported that the nanofluid generates a very fast $T_{2gm}$ of approximately 0.8 ms due to the presence of the iron as well as the significant surface relaxation arising from the specific surface area. As shown in Figure 10a1, the fresh Pickering nanoemulsion shows a similar $T_2$ to the nanofluid. Figure 10b1 shows that the two peaks in the NMR relaxation distribution are observed as the Pickering nanoemulsion ages for 4 days. This is caused by the thin layer of creaming at the top of the system, as shown in Figure 10b3. In addition, the original $T_2$ distribution shifts toward a faster $T_{2gm}$ of around 0.5 ms, with the other new peak exhibiting $T_{2gm}$ of approximately 1.0 ms. It is the concentration of the nanoparticles (refer to Section S5 in the Supporting Information) and droplet size that affects the $T_2$ distributions. When the aging time is extended to 35 days, the $T_2$ of the aqueous phase (i.e., nanoemulsion and nanofluid) becomes faster, with a correspondingly slow $T_2$ for the hydrocarbon phase (i.e., creaming and pure hydrocarbon). The smaller $T_2$ of the hydrocarbon phase in the Pickering emulsion than that of the bulk of pure hydrocarbon is caused by the surface relaxation, in terms of eq 1. At the end of the measurements, the $T_2$ of the aqueous phase reaches $T_{2gm}$ of approximately 0.2


https://doi.org/10.1021/acs.langmuir.3c00133
Langmuir 2023, 39, 6975−6991

ms while the creaming generates a $T_{2gm}$ of around 200 ms, as shown in Figure 10d1. Furthermore, there is another new peak occurring under the distribution of the bulk of pure hydrocarbon. This results from the fact that the pure hydrocarbon is generated at the top of the nanoemulsion system, as shown in Figure 10d3.

The NMR relaxation distributions for the Classical nanoemulsion instability are reported in Figure 11. The relaxation distributions of the Classical nanoemulsions are compared to the polymer solution (continuous media) and the hydrocarbon (dispersed phase). Figure 10a−d shows the Classical nanoemulsion aging for 0 h (i.e., immediately after the emulsification), 4 days, 35 days, and 60 days, respectively. The Classical nanoemulsion shows a $T_2$ distribution ranging between the polymer solution and the bulk of the pure hydrocarbon. As the Classical nanoemulsion becomes unstable, the other peak occurs, representing the oil phase with the aqueous phase shifting toward $T_2$ of the polymer solution. The relaxation times of the aqueous phase increase because, as the droplet sizes grow and phase separation takes place, the interfacial area diminishes, and the contribution of surface relaxation to the decay of magnetization is reduced.

In terms of eq 8, the evolutional section heights for different nanoemulsions can be calculated from NMR relaxometry and are shown in Figure 12, in comparison with the X-ray CT imaging and theoretical modeling results. Figure 12a−d shows the Pickering nanoemulsions with different hydrocarbons, Pickering nanoemulsions with different emulsification energies, Classical nanoemulsions with different hydrocarbons, and Classical nanoemulsions with different emulsification energies, respectively. Figure 12 shows that the modeling results reach good agreement with the experimentally measured results from NMR relaxometry and X-ray CT imaging. It is shown that the volume fraction of the aqueous phase decreases with a corresponding increase in the volume fraction of the oil phase. It should be noted that the aqueous phase includes nanofluid/polymer solution and nanoemulsion, while the oil phase comprises creaming and free oil. Generally, the oil phase increases as a function of aging time until a critical aging time and maintains the volume fraction to the end of the tests, showing that the phases are separated. For Pickering nanoemulsion synthesized with $C_{16}H_{34}$, it is still in the instability process without reaching the critical aging days for phase separation, which is the best stable nanoemulsion among the 16 different nanoemulsions. In comparison with the Classical nanoemulsions, Pickering nanoemulsions have a longer critical aging time to reach the plateau with a correspondingly slower creaming rate, hence better stability. This can be explained by the fact that the attachment of nanoparticles onto a droplet surface decreases the mass transfer coefficient for molecules to transport from the bulk aqueous phase into other droplets.[38] In addition, an emulsified hydrocarbon with low solubility in the aqueous phase exhibits a slower creaming rate due to the inhibited Ostwald ripening. It should be noted that the alkene of $C_{18}H_{36}$ has a greater solubility than the alkane of $C_{16}H_{34}$ and therefore the nanoemulsions with $C_{16}H_{34}$ show better stability even though the carbon chain is shorter than $C_{18}H_{36}$. Furthermore, emulsification energy also affects the creaming rate due to the resultant size distribution. A too small emulsification energy may contribute to incomplete emulsification, leaving most of the droplets uncovered by the emulsifiers, while a too strong emulsification energy may produce some small droplets with wide distribution, which enhances the Ostwald ripening and flocculation. This results in a greater creaming rate, compared to the optimum emulsification energy, which generates moderate droplets with narrow distribution.

Overall, the functionality of low-field NMR and X-ray CT imaging for the advanced characterization of complex fluids is summarized in Table 1. Low-field NMR relaxometry can provide an analysis of the viscosity, droplet size distribution, and composition of complex fluids.[27,56,57] X-ray CT imaging provides a spatiotemporal profile of substances with different differences. Both techniques are simple, fast, non-destructive, and capable of yielding an incredible wealth of information in a complementary method. The samples can be directly tested without any specific preparations. In addition, both sensors are not influenced by the optical or dielectric properties of the system. The validation results of NMR and X-ray CT confirm the accuracy of both techniques, thus providing the NMR as an alternative method for the potential field application for compositional analysis. Both techniques can extend the applications for the investigation of complex fluids, such as emulsions, foams, and suspensions.

**Table 1. Functionality of Low-Field NMR and X-ray CT Imaging for Characterization of Complex Fluids[a]**

| functionality | NMR | X-ray CT |
|---|---|---|
| hydrocarbon volume profile | no | **yes** |
| evolutional hydrocarbon volume | **yes** | **yes** |
| evolutional droplet size distribution | **yes** | no |
| non-destruction of the samples | **yes** | **yes** |
| specific preparation of the samples | **no** | **no** |
| test time | 10−300 s[b] | ∼10 s or even less[c] |

[a]Bold fonts represent the advantages of the techniques. [b]Time depends on the components that may affect the CPMG spin-echo train. [c]Time depends on the resolution and number of samples.

**Theoretical Analysis of the Creaming on Nanoemulsions.** Figure 13 shows the comparisons of the theoretical creaming rates with experimental results. theoretical creaming rates with experimentally measured results by utilizing low-field NMR and X-ray CT imaging techniques. The newly proposed theoretical model agrees well with the experimentally obtained results. However, the Stokes' law coupled with the classical LSW theory underestimates the creaming rate. This is caused by the underestimated coarsening rates predicted by the classical LSW theory,[19,39,55] which neglects the effect of the volume fraction of the dispersed

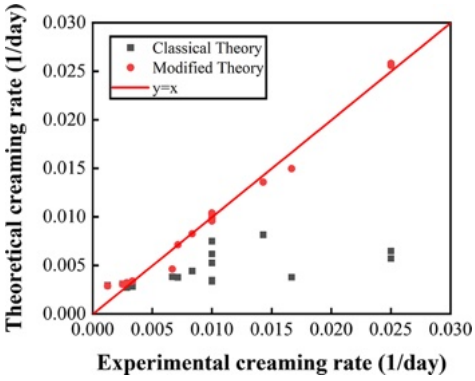


**Figure 13.** Comparisons of the theoretical creaming rates with experimental results.


https://doi.org/10.1021/acs.langmuir.3c00133
Langmuir 2023, 39, 6975−6991

phase, size distribution, and flocculation. In addition, Weiss et al.[39] invoked the enhanced transport via micelles that solubilize the hydrocarbons.

In short, our model reveals that the Ostwald ripening along with flocculation enhances the nanoemulsion creaming by increasing the droplet size. The attachment of nanoparticles onto a droplet surface decreases the mass transfer coefficient[38] for hydrocarbon molecules to move from the bulk aqueous phase into other droplets, thus slowing the Ostwald ripening. Therefore, Pickering nanoemulsions show a better stability behavior compared to Classical nanoemulsions. The emulsified hydrocarbon with low solubility in the aqueous phase exhibits a slower coarsening rate, and therefore better stability, relative to the emulsified hydrocarbon with high solubility. In addition, a moderate droplet size with narrow distribution is helpful to reduce the difference of chemical potentials among the droplets, hence preventing the Ostwald ripening and resulting in better stability compared to a small droplet size with a very wide distribution. The newly proposed model also implies that Pickering nanodroplets without any other surface active agents (e.g., surfactants, polymers, alkalis, etc.) may reach thermodynamic stability when the following conditions are met: (i) The dispersed hydrocarbon has a solubility with an order of less than $10^{-7}$ kg/m$^3$(e.g., heavy hydrocarbons); (ii) the nanodroplets are fully covered by the nanoparticles in terms of eq S4 (by addition of high concentrations of nanoparticles); and (iii) the size of the nanodroplets are sufficiently small to overcome the Brownian diffusion. This theory is experimentally verified by Sacanna et al.,[58] where they used magnetite to spontaneously emulsify and thermodynamically stabilize 3-methacryloxypropyl trimethoxysilane with sizes distributed between 30 and 150 nm.

## CONCLUSIONS

In this study, we synthesize and stabilize nanodroplets solely by Pickering nanoparticles and compare their instability with the Classical nanoemulsions from experimental and theoretical perspectives. The main points can be drawn as below:

(1) The Stokes' law[46] coupled with the classical Lifshitz–Slyozov–Wagner theory[36,37] underestimates the creaming rate due to the depreciated coarsening rate.[19,39,55] We develop a new creaming theory by incorporating the effects of hydrocarbon types, volume fraction, droplet size distribution, flocculation, and Pickering nanoparticles. The theoretical modeling results match well with the creaming rates obtained from NMR and X-ray CT imaging.

(2) Experimental and theoretical modeling results reveal that the Ostwald ripening is the main instability mechanism for nanoemulsions due to the very small droplets associated with a high surface area.[11,19,20] The insolubility of long-chain hydrocarbons in water acts as a kinetic barrier to Ostwald ripening, making those nanoemulsions, both the Pickering and Classical ones, inherently stable to Ostwald ripening. The polydisperse nanoemulsions are more easily separated due to the severely inhomogeneous chemical potentials of the emulsion droplets.

(3) Compared to the Classical nanoemulsions, Pickering nanoemulsions show much stronger stability against gravity separation, flocculation, Ostwald ripening, and coalescence. This is caused by the fact that the attachment of nanoparticles onto a droplet surface decreases the mass transfer of hydrocarbon molecules to transport from the bulk aqueous phase into other droplets.[38]

(4) This study demonstrates that NMR relaxometry and X-ray CT imaging are complementary for the quantitative analysis of the instability of complex fluids. X-ray CT quantifies the spatiotemporal hydrocarbon volume distribution within the system, while the low-field NMR relaxometry contributes to the component volume fraction. The gravity separation results obtained from the NMR and X-ray CT reach good agreement.

This work improves the understanding of the instability of the Pickering and Classical nanoemulsions, setting the stage for subsequent tests on these nanodroplets. The newly designed experimental approaches and newly developed theory may satisfy the essential stability evaluation in various industries, such as food, cosmetics, biomedicine, agrochemistry, and petrochemistry.[59−61]

## ASSOCIATED CONTENT

### Supporting Information

The Supporting Information is available free of charge at https://pubs.acs.org/doi/10.1021/acs.langmuir.3c00133.

Parameters for theoretical calculation; hydrocarbon profile of nanoemulsion by X-ray CT imaging; NMR relaxation distributions for nanoemulsions; calculation of density of the Pickering nanodroplets; characterization of iron oxide nanoparticles; and comparisons of low-field NMR and X-ray CT for characterization of complex fluids (including experimental data and numerical coefficients for theoretical modeling, spatiotemporal hydrocarbon profiles, relaxation distributions, $T_{2gm}$ as a function of different concentrations, and comparisons of the NMR and X-ray CT measured phase volumes) (PDF)

## AUTHOR INFORMATION


### Corresponding Authors

**Boxin Ding** − *Department of Chemical and Petroleum Engineering, University of Calgary, Calgary, AB T2N 1N4, Canada; Reservoir Engineering Research Institute, Palo Alto, California 94301, United States;* orcid.org/0000-0001-8344-8465; Email: boxin.ding@ucalgary.ca

**Steven L. Bryant** − *Department of Chemical and Petroleum Engineering, University of Calgary, Calgary, AB T2N 1N4, Canada; Canada Excellence Research Chair in Materials Engineering for Unconventional Oil Reservoirs, Calgary, AB T2N 1N4, Canada;* orcid.org/0000-0002-7547-0475; Email: steven.bryant@ucalgary.ca

**Apostolos Kantzas** − *Department of Chemical and Petroleum Engineering, University of Calgary, Calgary, AB T2N 1N4, Canada; TIPM Laboratory, PERM Inc., Calgary, AB T2E 6P2, Canada*; Email: akantzas@ucalgary.ca

### Authors

**Seyedeh Hannaneh Ahmadi** − *Department of Chemical and Petroleum Engineering, University of Calgary, Calgary, AB T2N 1N4, Canada*

**Petro Babak** − *Department of Chemical and Petroleum Engineering, University of Calgary, Calgary, AB T2N 1N4,*

*Canada; Southern Alberta Institute of Technology, Calgary, AB T2M 0L4, Canada;* orcid.org/0000-0002-5501-7075

Complete contact information is available at: https://pubs.acs.org/10.1021/acs.langmuir.3c00133

### Notes

The authors declare no competing financial interest.

## ■ ACKNOWLEDGMENTS

This research was undertaken thanks in part to funding from the Canada First Research Excellence Fund (CFREF) Program and the Canada Excellence Research Chairs (CERC) Program. The authors acknowledge the Dynamic Imaging Lab (DIL) and Microscopy & Imaging Facility (MIF) at the University of Calgary. Brian Baillie from the CERC lab, Dr. Chris Debuhr from the DIL, and Dr. Priyanka Mukherjee from MIF are greatly acknowledged for their help in ICP-MS, CryoSEM, and TEM tests, respectively. B.D. would like to thank Dr. Abbas Firoozabadi at Rice University, Dr. Ke Xu at Peking University, and Dr. Changqian Cao at Chinese Academy of Sciences for their helpful and insightful discussions.

## ■ NOMENCLATURE

### Abbreviations

| | |
|---|---|
| CT | computed tomography |
| CPMG | Carr−Purcell−Meiboom−Gill |
| CryoSEM | scanning electron cryomicroscopy |
| DLS | dynamic light scattering |
| DLVO | Derjaguin−Landau−Verwey−Overbeek |
| IONP | iron oxide nanoparticle |
| ICP-MS | inductively coupled plasma-mass spectrometry |
| IFT | interfacial tension |
| LSW | Lifshitz, Slezov, and Wagner |
| NE | pulse number |
| NMR | nuclear magnetic resonance |
| O/W | oil-in-water |
| PIONP | polymer-coated iron oxide nanoparticle |
| P/N | polymer-to-nanoparticle |
| TGA | thermogravimetric analysis |
| TEM | transmission electron microscopy |
| TE | echo time |
| TW | waiting time |
| W/O | water-in-oil |

### Greek symbols

| | |
|---|---|
| $\varepsilon$ | permittivity of water |
| $\lambda$ | average covering coefficient |
| $\mu_o$ | oil viscosity |
| $\xi_n$ | normalized density |
| $\rho$ | density of the fluid |
| $\rho_m$ | calculated density of the mixed phase (i.e., nanoemulsion) from the CT slices |
| $\rho_d$ | density of the dispersed phase |
| $\rho_c$ | density of the continuous phase |
| $\sigma$ | interfacial tension between the dispersed droplets and continuous medium |
| $\phi_o$ | hydrocarbon volume fraction of the nanoemulsion |
| $\psi_0$ | surface potential |

### Variables

| | |
|---|---|
| A | interfacial area |
| $A_H$ | Hamaker constant for colloidal dispersion |
| AP | amplitude of the fluid signal |
| $C$ | coalescence rate |
| $D$ | diffusion coefficient of the dispersed phase in the continuous phase |
| $E_t$ | net potential energy for the interaction between two droplets |
| $E_d$ | van der Waals attractive energy |
| $E_e$ | repulsive electrostatic energy |
| $G$ | Gibbs free energy |
| $g$ | gravity acceleration |
| $H$ | surface-to-surface separation between the droplets |
| $I$ | amplitude index |
| $K$ | strength of surface relaxation |
| $k$ | inverse Debye length (or the reciprocal of the double layer thickness) |
| $n$ | droplet number after coalescence |
| $n_0$ | number of droplets immediately after emulsification |
| $R$ | gas constant |
| $r$ | droplet radius |
| $r_0$ | original size of the emulsion droplets |
| $S_\infty$ | solubility of the hydrocarbon |
| $T$ | temperature |
| $T_2$ | transverse relaxation time |
| $T_{2bulk}$ | relaxation time of bulk fluid |
| $T_{2surface}$ | relaxation time resulting from surface relaxation |
| $t$ | aging time |
| $t_c$ | time when the droplet size reaches the critical size |
| $V_m$ | volume of the mixed phase |
| $V_d$ | volume of the dispersed phase |
| $V_c$ | volume of the continuous phase |
| $V$ | volume of the fluid |
| $v_m$ | molar volume of the dispersed phase |

## ■ REFERENCES

(1) Galus, S.; Kadzińska, J. Food applications of emulsion-based edible films and coatings. *Trends Food Sci. Technol.* **2015**, *45*, 273−283.

(2) Singh, Y.; Meher, J. G.; Raval, K.; Khan, F. A.; Chaurasia, M.; Jain, N. K.; Chourasia, M. K. Nanoemulsion: Concepts, development and applications in drug delivery. *J. Controlled Release* **2017**, *252*, 28−49.

(3) Ramsburg, C. A.; Pennell, K. D.; Kibbey, T. C. G.; Hayes, K. F. Use of a Surfactant-Stabilized Emulsion To Deliver 1-Butanol for Density-Modified Displacement of Trichloroethene. *Environ. Sci. Technol.* **2003**, *37*, 4246−4253.

(4) Sonneville-Aubrun, O.; Simonnet, J. T.; L'Alloret, F. Nanoemulsions: a new vehicle for skincare products. *Adv. Colloid Interface Sci.* **2004**, *108-109*, 145−149.

(5) Ding, B.; Dong, M.; Chen, Z.; Kantzas, A. Enhanced oil recovery by emulsion injection in heterogeneous heavy oil reservoirs: Experiments, modeling and reservoir simulation. *J. Pet. Sci. Eng.* **2022**, *209*, 109882.

(6) Ding, B.; Nie, Z.; Li, Z.; Dong, M. Emulsion-assisted thermal recovery method in heterogeneous oilsands reservoir. *J. Pet. Sci. Eng.* **2021**, *197*, 108113.

(7) Ding, B.; Sang, Q.; Nie, Z.; Li, Z.; Dong, M.; Chen, Z.; Kantzas, A. An Improved Study of Emulsion Flooding for Conformance Control in a Heterogeneous 2D Model with Lean Zones. *Spe J.* **2021**, *26*, 3094−3108.

(8) Firoozabadi, A. *Thermodynamics and applications in hydrocarbon energy production*; McGraw-Hill Education, 2016. 10−15.

(9) Nakajima, H.; Tomomossa, S.; Okabe, M. *First Emulsion Conference*. Paris, France, 1993.

(10) Nakajima, H. Microemulsions in cosmetics. *Surfactant Sci. Ser.* **1997**, *66*, 175−197.

(11) Tadros, T.; Izquierdo, P.; Esquena, J.; Solans, C. Formation and stability of nano-emulsions. *Adv. Colloid Interface Sci.* **2004**, *108-109*, 303−318.

(12) Gupta, A.; Eral, H. B.; Hatton, T. A.; Doyle, P. S. Nanoemulsions: formation, properties and applications. *Soft Matter* **2016**, *12*, 2826−2841.
(13) He, B.; He, J.; Bi, E.; Zou, H.; Liu, T.; Liu, Z. Transport and retention of nano emulsified vegetable oil in porous media: Effect of pore straining, roughness wedging, and interfacial effects. *J. Environ. Manage.* **2022**, *320*, 115912.
(14) McClements, D. J. Nanoemulsions versus microemulsions: terminology, differences, and similarities. *Soft Matter* **2012**, *8*, 1719−1729.
(15) Pickering, S. U. Cxcvi.—emulsions. *J. Chem. Soc.* **1907**, *91*, 2001−2021.
(16) Watson, D. B.; Wu, W. M.; Mehlhorn, T.; Tang, G.; Earles, J.; Lowe, K.; et al. In situ bioremediation of uranium with emulsified vegetable oil as the electron donor. *Environ. Sci. Technol.* **2013**, *47*, 6440−6448.
(17) Melle, S.; Lask, M.; Fuller, G. G. Pickering emulsions with controllable stability. *Langmuir* **2005**, *21*, 2158−2162.
(18) Ding, B.; Bryant, S.L.; Kantzas, A. Magnetic Nanoemulsions for Fluid Conductivity Analysis in Subsurface Reservoirs. U.S. 63/354,138. 2022.
(19) Wooster, T. J.; Golding, M.; Sanguansri, P. Impact of oil type on nanoemulsion formation and Ostwald ripening stability. *Langmuir* **2008**, *24*, 12758−12765.
(20) Solans, C.; Izquierdo, P.; Nolla, J.; Azemar, N.; Garcia-Celma, M. J. Nano-emulsions. *Curr. Opin. Colloid Interface Sci.* **2005**, *10*, 102−110.
(21) Ding, B.; Dong, M. Optimization of plugging high mobility zones in oil sands by injection of oil-in-water emulsion: Experimental and modeling study. *Fuel* **2019**, *257*, 116024.
(22) Ding, B.; Yu, L.; Dong, M.; Gates, I. Study of conformance control in oil sands by oil-in-water emulsion injection using heterogeneous parallel-sandpack models. *Fuel* **2019**, *244*, 335−351.
(23) Yu, L.; Ding, B. X.; Dong, M. Z.; Jiang, Q. Plugging Ability of Oil-in-Water Emulsions in Porous Media: Experimental and Modeling Study. *Ind. Eng. Chem. Res.* **2018**, *57*, 14795−14808.
(24) Yu, L.; Dong, M. Z.; Ding, B. X.; Yuan, Y. G. Experimental study on the effect of interfacial tension on the conformance control of oil-in-water emulsions in heterogeneous oil sands reservoirs. *Chem. Eng. Sci.* **2018**, *189*, 165−178.
(25) Yu, L.; Dong, M. Z.; Ding, B. X.; Yuan, Y. G. Emulsification of heavy crude oil in brine and its plugging performance in porous media. *Chem. Eng. Sci.* **2018**, *178*, 335−347.
(26) Ahmadi, S.H.; Ding, B.; Bryant, S. L.; Kantzas, A. Synthesis and Characterization of Magnetic Nanodroplets for Flowback Analysis in Fractured Reservoirs. In *SPE Canadian Energy Technology Conference and Exhibition*, 2023; OnePetro.
(27) Peña, A. A.; Hirasaki, G. J. Enhanced characterization of oilfield emulsions via NMR diffusion and transverse relaxation experiments. *Adv. Colloid Interface Sci.* **2003**, *105*, 103−150.
(28) Jiang, T. M.; Hirasaki, G.; Miller, C.; Moran, K.; Fleury, M. Diluted bitumen water-in-oil emulsion stability and characterization by nuclear magnetic resonance (NMR) measurements. *Energy Fuels* **2007**, *21*, 1325−1336.
(29) Opedal, N. V. D. T.; Sørland, G.; Sjöblom, J. Emulsion Stability Studied by Nuclear Magnetic Resonance (NMR). *Energy Fuels* **2010**, *24*, 3628−3633.
(30) Kenyon, W. Petrophysical principles of applications of NMR logging. *log anal.* **1997**, *38* ().
(31) McClements, D. J. Critical review of techniques and methodologies for characterization of emulsion stability. *Crit. Rev. Food Sci. Nutr.* **2007**, *47*, 611−649.
(32) Wen, Y. W.; Kantzas, A. Monitoring bitumen-solvent interactions with low-field nuclear magnetic resonance and X-ray computer-assisted tomography. *Energy Fuels* **2005**, *19*, 1319−1326.
(33) Cao, C.; Abdelphata, E.; Meimanova, A.; Wang, J.; Yu, J.; Pilapil, B.et al. Hierarchical stabilization of emulsions with multi- scale interconnected droplets and ultra-low nanoparticle loadings. *Res. Square* **2021**.
(34) Kantzas, A. Investigation of physical properties of porous rocks and fluid flow phenomena in porous media using computer assisted tomography. *In Situ;(USA)* **1990**, *14* ().
(35) Ding, B.; Shi, L.; Babak, P. *A Method for Interpretation and Reconstruction of X-ray CT Imaging for Multiphase Flow in Porous Media*. Zenodo. July 1, 2022, DOI: 10.5281/zenodo.6789204.
(36) Lifshitz, I. M.; Slyozov, V. V. The kinetics of precipitation from supersaturated solid solutions. *J. Phys. Chem. Solids* **1961**, *19*, 35−50.
(37) Wagner, C. Theorie der alterung von niederschlägen durch umlösen (Ostwald-reifung). *Zeitschrift für Elektrochemie, Berichte der Bunsengesellschaft für physikalische Chemie* **1961**, *65*, 581−591.
(38) Yang, Z. *Diffusion and Mass Transfer of Gases in Surfactant Solutions and Nanofluids*. 2020.
(39) Weiss, J.; Herrmann, N.; McClements, D. J. Ostwald ripening of hydrocarbon emulsion droplets in surfactant solutions. *Langmuir* **1999**, *15*, 6652−6657.
(40) Verwey, E. J. W. Theory of the stability of lyophobic colloids. *J. Phys. Chem.* **1947**, *51*, 631−636.
(41) Derjaguin, B.; Landau, L. Theory of the stability of strongly charged lyophobic sols and of the adhesion of strongly charged particles in solutions of electrolytes. *Prog. Surf. Sci.* **1993**, *43*, 30−59.
(42) Tadros, T. Application of rheology for assessment and prediction of the long-term physical stability of emulsions. *Adv. Colloid Interface Sci.* **2004**, *108-109*, 227−258.
(43) Borwankar, R. P.; Lobo, L. A.; Wasan, D. T. Emulsion stability — kinetics of flocculation and coalescence. *Colloids Surf.* **1992**, *69*, 135−146.
(44) Kabalnov, A. S.; Makarov, K. N.; Pertzov, A. V.; Shchukin, E. D. Ostwald Ripening in Emulsions . 2. Ostwald Ripening in Hydrocarbon Emulsions - Experimental-Verification of Equation for Absolute Rates. *J. Colloid Interface Sci.* **1990**, *138*, 98−104.
(45) Li, J.; Guo, C.; Ma, Y.; Wang, Z.; Wang, J. Effect of initial particle size distribution on the dynamics of transient Ostwald ripening: A phase field study. *Acta Mater.* **2015**, *90*, 10−26.
(46) Miller, C. C. The Stokes-Einstein law for diffusion in solution. *Proc. R. Soc. London, Ser. A* **1924**, *106*, 724−749.
(47) Ding, B.; Dong, M.; Yu, L. A model of emulsion plugging ability in sandpacks: Yield pressure drop and consistency parameter. *Chem. Eng. Sci.* **2020**, *211*, 115248.
(48) Brooks, R. A.; Di Chiro, G. Beam hardening in x-ray reconstructive tomography. *Phys. Med. Biol.* **1976**, *21*, 390.
(49) Taylor, G. I. The instability of liquid surfaces when accelerated in a direction perpendicular to their planes I. *Proc. R. Soc. London, Ser. A* **1950**, *201*, 192−196.
(50) Rayleigh, R. Investigation of the character of the equilibrium of an incompressible heavy fluid of variable density. *Proc. London Math. Soc.* **1882**, *1*, 170−177.
(51) Aveyard, R.; Binks, B. P.; Clint, J. H. Emulsions stabilised solely by colloidal particles. *Adv. Colloid Interface Sci.* **2003**, *100-102*, 503−546.
(52) Horozov, T. S.; Binks, B. P. Particle-Stabilized Emulsions: A Bilayer or a Bridging Monolayer? *Am. Ethnol.* **2006**, *118*, 787−790.
(53) Binks, B. P. Particles as surfactants - similarities and differences. *Curr. Opin. Colloid Interface Sci.* **2002**, *7*, 21−41.
(54) Taylor, P. Ostwald ripening in emulsions. *Adv. Colloid Interface Sci.* **1998**, *75*, 107−163.
(55) Thompson, K. L.; Derry, M. J.; Hatton, F. L.; Armes, S. P. Long-Term Stability of n-Alkane-in-Water Pickering Nanoemulsions: Effect of Aqueous Solubility of Droplet Phase on Ostwald Ripening. *Langmuir* **2018**, *34*, 9289−9297.
(56) Johns, M. L. NMR studies of emulsions. *Curr. Opin. Colloid Interface Sci.* **2009**, *14*, 178−183.
(57) Bryan, J.; Kantzas, A.; Bellehumeur, C. Oil-viscosity predictions from low-field NMR measurements. *SPE Reservoir Eval. Eng.* **2005**, *8*, 44−52.
(58) Sacanna, S.; Kegel, W. K.; Philipse, A. P. Thermodynamically stable pickering emulsions. *Phys. Rev. Lett.* **2007**, *98*, 158301.
(59) Ding, B.; Shi, L.; Dong, M. *Development And Application Of Emulsion-based Conformance Control Method For Enhanced Bitumen*

*Recovery By Steam-assisted Gravity Drainage*. In Day 4 Thu, October 29, 2020, Virtual; Paper SPE-201568-MS, 2020.
(60) Ding, B.; Shi, L.; Dong, M. Conformance control in heterogeneous two-dimensional sandpacks by injection of oil-in-water emulsion: Theory and experiments. *Fuel* **2020**, *273*, 117751.
(61) Yu, L.; Ding, B.; Dong, M.; Jiang, Q. A new model of emulsion flow in porous media for conformance control. *Fuel* **2019**, *241*, 53−64.





https://doi.org/10.1021/acs.langmuir.3c00133
*Langmuir* 2023, 39, 6975−6991